

Evolution of action-space coherence in a Milky Way-like simulation

Arunima Arunima¹*, Mark R. Krumholz¹, Michael J. Ireland¹, Chuhan Zhang¹ and Sven Buder¹

¹Research School of Astronomy and Astrophysics, Australian National University, Canberra ACT 2601, Australia

Accepted XXX. Received YYY; in original form ZZZ

ABSTRACT

Efforts to dynamically trace stars back to the now-dissolved clusters in which they formed rely implicitly on the assumption that stellar orbital actions are conserved. While this holds in a static, axisymmetric potential, it is unknown how strongly the time-varying, non-axisymmetric structure of a real galactic disk drives action drift that inhibits cluster reconstruction. We answer this question using a high-resolution magnetohydrodynamic simulation of a Milky Way-like spiral disc galaxy. We show that, while stars experience significant action evolution over $\lesssim 100$ Myr, they do so in a correlated fashion whereby stars born in close proximity maintain very similar actions for up to 0.5 Gyr. The degree of coherence shows no significant dependence on galactocentric radius, but varies between action components: vertical actions decohere for stars born more than a few hundred parsecs apart (likely due to giant molecular clouds), while radial and azimuthal actions remain correlated on kiloparsec scales (likely influenced by spiral arms). We use our measurements of the rate of action decoherence to develop a probabilistic framework that lets us infer the initial sizes of the star cluster progenitors of present-day stellar streams from their measured action distributions, which we apply to 438 known moving groups. Our results suggest that most of these streams likely originated from compact clusters, but that a significant minority are instead likely to be resonant or dynamically induced structures. This method of classifying streams complements existing methods, optimises the use of expensive spectroscopic abundance measurements, and will be enhanced by the more precise kinematic data that will soon become available from *Gaia* DR4.

Key words: Galaxy: kinematics and dynamics – astrometry

1 INTRODUCTION

Stars form in clustered environments inside giant molecular clouds (GMCs), inheriting mutually similar kinematics and chemical compositions from their shared birth material (Lada & Lada 2003). Most of this clustered structure is not gravitationally bound following dispersal of the star-forming gas, and dissolves within tens to hundreds of million years (Myr) leaving the stellar population dispersed in the Galactic field. Even after the stars disperse in physical space, however, they retain imprints of their birthplaces in their characteristics (Freeman & Bland-Hawthorn 2002). If the dispersal occurs in a smooth, axisymmetric, and time-static potential, orbital actions are among these imprints, as they are expected to remain adiabatic invariants under motion in a potential satisfying these conditions (Binney & Tremaine 2008). These conserved quantities have, hence, become central to dynamical studies and Galactic archaeology: if stars born together remain clustered in action space, then action-based co-natal tagging can become a powerful tool for mapping the star formation history of the Galaxy (Helmi et al. 2018; Myeong et al. 2019; Zucker et al. 2022; Swiggum et al. 2025).

However, the Milky Way potential is neither static nor axisymmetric. It is shaped by both external perturbations such as satellite interactions (Antoja et al. 2018, 2023; Frankel et al. 2023) and secular internal processes such as transient spiral arm structure, the rotating

Galactic bar, and the formation and dispersal of GMCs (Sellwood & Binney 2002; Roškar et al. 2008; Fragkoudi et al. 2019; Mackereth et al. 2019; Tremaine et al. 2023). These processes all contribute to a time-variable and non-axisymmetric component of the potential that can perturb stellar actions. Numerical simulations have confirmed this non-conservation of actions across a range of models: from N -body simulations without gas dynamics or star formation, the least realistic representations of the Galaxy (Solway et al. 2012; Vera-Ciro et al. 2014; Mikkola et al. 2020), to semi-analytic dynamical models (Kamdar et al. 2021), and most recently and realistically, to fully self-consistent magnetohydrodynamical (MHD) simulations that include star formation, feedback and live disc with flocculent spiral arms (Tepper-García et al. 2022, 2025; Arunima et al. 2025, hereafter Paper I).

In Paper I, we quantified the non-conservation of individual stellar actions and showed that actions undergo a logarithmic random walk over timescales of hundreds of Myr. Yet a fundamental question still remains unanswered: Do co-natal stars retain coherence in action space over longer timescales? That is, while individual stars' actions undergo random walks that significantly change their values over timescales of ~ 100 Myr, is it possible that the random walks taken by stars that are born close together are *correlated*, so that their actions remain close together in action space for longer times? There are compelling reasons to expect they might be. Co-natal stars, having shared initial conditions and experiencing same gravitational perturbations, should show similar changes in their actions and remain

* E-mail: arunima.arunima@anu.edu.au

clustered in action space. If such coherence persists, it would lend strong support to the use of actions for co-natal tagging, providing a robust tool for identifying disrupted clusters.

Indeed, several earlier studies have found evidence of long-lived clustering in phase space or integral-of-motion space even after spatial phase mixing. N -body studies of disrupting satellite galaxies or clusters have shown that stars can remain tightly grouped in action space for many orbital periods (Helmi & de Zeeuw 2000; Gómez & Helmi 2010). Using cosmological hydrodynamical simulations, Arora et al. (2022) demonstrated that stars born close together in the FIRE-2 Milky Way analogue retain action-space coherence for several hundred Myr before gradual dispersion in an evolving potential. Similarly, Kamdar et al. (2019) modelled clustered star formation with realistic Galactic potential and found that co-natal stars maintain correlated kinematic signatures for extended timescales. Observationally, recent studies using *Gaia* have identified groups with dynamical coherence indicative of common origin due to their chemical and age similarities (Coronado et al. 2020; Fürnkranz et al. 2024). These results suggest that actions indeed hold promise as diagnostics of star-formation origins, but their utility depends on timescales, birth separation, and the dynamical environment. Despite these advances, no study has yet examined the evolution of co-natal action coherence in a high-resolution, self-consistent MHD simulation of a live Milky Way-like disc. This gap leaves open uncertainties in how reliably actions can be used as archaeological tracers of stellar birth origins.

In this paper, we address this question using a high-resolution MHD simulation of a Milky Way-like disc galaxy. Building directly on our previous study of individual stars' action diffusion, we aim to extend the study of evolution of stellar actions for pairs of stars. This allows us to quantify the evolution of action differences and to measure the characteristic timescales and physical scales over which stars lose dynamical coherence in action space (a process we refer to as action-space decoherence). Through this, we can infer the co-natal origin of stars based solely on their current dynamical separation – which is easier than ever to achieve thanks to immaculate astrometric information from *Gaia* DR3 (Gaia Collaboration et al. 2023), with the promise of even better data from *Gaia* DR4 in the very near future. Hence, we explore the use of our insights for observational analysis of star cluster disruption, stellar streams, dynamical reconstruction of co-natal groups in the Galactic disc.

The paper is organised as follows. In Section 2, we describe the galactic simulation and methodology used in this study. In Section 3, we present the main results from this study including temporal evolution of action differences for pairs of stars, scales of decoherence as well as dependence of this evolution on the stars' birth environment. In Section 4, we outline an observational application of our findings to astrometric data from *Gaia* and spectroscopic surveys, which should allow for inferences of birth conditions of moving groups and stellar streams in the Milky Way disc. Finally, in Section 5, we summarise our key results and discuss their implications.

2 METHODS

2.1 Simulation

We use the same high-resolution MHD simulation of an isolated Milky Way-like disc galaxy previously employed in Paper I. This simulation, originally introduced by Zhang et al. (2025, hereafter Z25), is an extension of the full galaxy zoom-in simulations described by Wibking & Krumholz (2023) and Hu et al. (2023) (hereafter

WK23 and H23, respectively). Here, we provide a brief summary of the simulation setup and refer readers to Paper I, WK23, H23 and Z25 for full details.

The simulation follows the evolution of a turbulent galactic disc under ideal MHD using the GIZMO code (Hopkins 2015, 2016; Hopkins & Raives 2016) with radiative cooling implemented via the GRACKLE library (Smith et al. 2017). Star formation occurs stochastically when the gas particle density ρ_g exceeds a critical threshold density ρ_{crit} ; for particles meeting this condition the probability of being converted to a star particle in a time step of size Δt is

$$P = 1 - \exp(-\epsilon_{\text{ff}} \Delta t / t_{\text{ff}}), \quad (1)$$

which corresponds to setting the star formation rate density to

$$\dot{\rho}_{\text{SFR}} = \epsilon_{\text{ff}} \frac{\rho_g}{t_{\text{ff}}}. \quad (2)$$

Here ϵ_{ff} is the star formation efficiency, ρ_g is the local gas density and

$$t_{\text{ff}} = \sqrt{\frac{3\pi}{32G\rho}} \quad (3)$$

is the local gas free-fall time. The critical threshold density ρ_{crit} is chosen to ensure that the local gravitational collapse is resolved, that is, the Jeans mass is nearly equal to the simulation mass resolution. The simulation uses a fixed efficiency per free fall time $\epsilon_{\text{ff}} = 0.01$, motivated from observations (Krumholz et al. 2019), increasing to $\epsilon_{\text{ff}} = 10^6$ for gas particles with $\rho_g \geq 100\rho_{\text{crit}}$; the latter choice is purely for numerical convenience, as it forces immediate conversion to star particles above this density threshold, thereby avoiding the extremely short timesteps that would otherwise be required in very dense gas.

The simulation mass resolution is high enough that stellar particles represent stellar populations too small to sample the full initial mass function (IMF), so the simulation treats stellar feedback on a star-by-star basis. When a star particle forms the code samples individual stars stochastically from a Chabrier (2005) IMF using the stellar population synthesis code SLUG (da Silva et al. 2012; Krumholz et al. 2015). Thereafter, SLUG computes the age-dependent internal properties of each star from the Padova stellar tracks (Bressan et al. 2012), and the corresponding ionising luminosity using the “starburst99” spectral synthesis method (Leitherer et al. 1999). The feedback module also uses SLUG to determine which stars end their lives as supernovae versus as AGB stars following the models of Sukhbold et al. (2016). The simulation deposits photoionisation and supernova feedback in the gas using the approaches described by Hopkins et al. (2018) and Armillotta et al. (2019), and returns mass and metals following the predictions of Sukhbold et al. (2016) for type II supernovae, Karakas & Lugaro (2016) for AGBs, and Doherty et al. (2014) for super-AGBs.

The simulation proceeds in two stages. The first phase, described in WK23, evolves an isolated galaxy from AGORA Milky Way-like initial conditions (Kim et al. 2016) using IMF-integrated feedback. The second phase is a high resolution re-simulation: using the 600 Myr snapshot from the WK23 simulation (which exhibits a stable gas fraction similar to the present day Milky Way), Z25 run the simulation for 100 Myr without enhancing the resolution but switching from the IMF-integrated treatment of feedback to the star-by-star feedback prescription described above. Then, the mass resolution is increased to $\Delta M \approx 300M_{\odot}$ using the particle splitting procedure outlined in H23 and the simulation continues for another 464 Myr, with snapshots output at 1 Myr intervals. By the end of the simulation, approximately 1.32 million star particles have formed. While

these particles represent small sub-cluster-scale populations rather than true individual stars, their masses are low enough that they should preserve the dynamical information imprinted at birth almost as well as individual stars. At the smallest scales, our simulation is expected to overestimate decoherence in action space due to star particles being significantly larger than median stellar masses.

2.2 Action calculation

Our first step in analysing these simulations is to compute actions for each star particle at each output time. Our full procedure for doing so, including several tests of the method, is provided in Section 3 and the Appendices of Paper I. We therefore only summarise here for reader convenience.

We calculate actions for the star particles using the epicyclic approximation, which is very accurate for young stars near the disc plane and is much more computationally efficient than alternative approaches. At each simulation snapshot, we use the gravitational potential computed by GIZMO at the position of each particle to construct an axisymmetric model for the galaxy's potential Φ . Following Binney & Tremaine (2008), we then decompose the stellar orbits into independent radial and vertical oscillations about a guiding centre at galactocentric radius R_g , characterised by the radial (κ) and vertical (ν) frequencies

$$\kappa^2 = \left(R \frac{\partial \Omega^2}{\partial R} + 4\Omega^2 \right)_{(R=R_g, z=0)} \quad (4)$$

$$\nu^2 = \left. \frac{\partial^2 \Phi}{\partial z^2} \right|_{(R=R_g, z=0)}, \quad (5)$$

where

$$\Omega(R) = \sqrt{\left. \frac{1}{R} \frac{\partial \Phi}{\partial R} \right|_{R, z=0}} \quad (6)$$

is the circular frequency.

To assign actions to each star, we first evaluate the stellar guiding centre from the star's angular momentum L_z by solving the implicit equation

$$|L_z| = R|v_\phi| = R_g^2 \Omega(R_g) \quad (7)$$

for R_g , where R is the star's radial position and v_ϕ its azimuthal velocity. From R_g we can immediately evaluate κ and ν from equation 4 and equation 5. We then compute the stellar radial, vertical, and azimuthal actions as

$$J_R = \frac{v_R^2 + \kappa^2(R - R_g)^2}{2\kappa} \quad (8)$$

$$J_z = \frac{v_z^2 + \nu^2 z^2}{2\nu} \quad (9)$$

$$J_\phi = L_z. \quad (10)$$

Finally, as mentioned in Paper I, many stars in the simulation are part of gravitationally bound clusters for at least some of their evolution, and the internal orbital motion within these clusters drives large variations in galactocentric actions. These can obscure the slower evolution induced by the Galactic potential, which is of primary concern here. To remove these short-timescale fluctuations, we apply a Butterworth low-pass filter with a cut-off frequency of $1/30 \text{ Myr}^{-1}$ to the action time series of each star. We use these filtered actions for all the analysis in this paper.

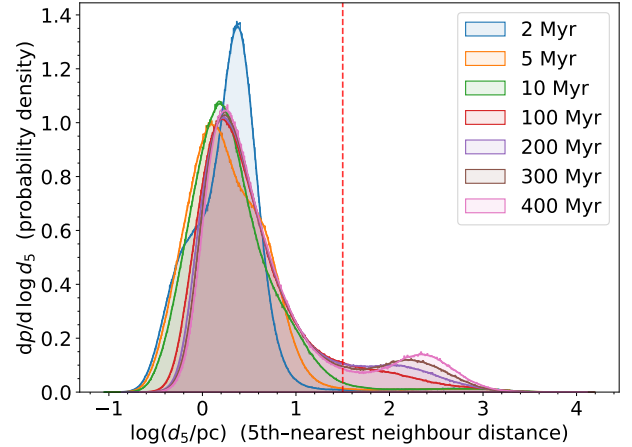


Figure 1. The distribution of 5th nearest neighbour distances d_5 for coeval stars at different ages (shown in the legend). We show the 30 pc limit that we use to separate cluster stars from dispersed stars as the red dashed vertical line.

2.3 Quantifying action-space coherence

The overarching goal of this work is to determine whether stars born together remain clustered in action space even as they drift apart in physical space. To this end, at each snapshot, we begin by identifying stars that were born together. We first identify stars that were born within the last 1 Myr and consider all pairs of two such stars. We group our pairs based on the physical distance between the two stars in the first snapshot in which the stars appear, d_{init} . We are interested in knowing how the distance in *action* between each pair of stars grows with the time Δt since their birth, as a function of their *physical* separation at birth d_{init} .

Before we can evaluate this, however, we must mitigate one important bias. Stars that are part of a gravitationally bound cluster will always remain clustered in action space simply because they are gravitationally bound to one another. We are therefore interested only in stars that have dispersed from their natal clusters. Thus our first challenge is to define a criterion by which we can identify dispersed stars. For this purpose, we examine the distribution of 5th nearest-neighbour distances for coeval stars – again defined as stars born in the same 1 Myr cohort – measured at various stellar ages. This is shown in Figure 1. Each cohort contains $N \approx 3000$ star particles, and the star-forming disc is roughly a cylinder $H \sim 200$ pc thick and $R \sim 5 - 10$ kpc in radius, so if the stars were randomly distributed we would expect the typical interstellar separation to be $\sim (\pi R^2 H / N)^{1/3} \sim 200$ pc. In fact we see that at all ages the peak of the fifth-nearest neighbour distance is much smaller than this, ~ 1 pc, reflecting that stars are clustered together. At the earliest ages the distribution of separations is unimodal and consists only of this clustered feature, but at later times a secondary feature peaking at $\gtrsim 100$ pc begins to appear, and the separation distribution becomes bimodal; the minimum between these two modes is at ≈ 30 pc. We therefore identify the small-separation peak with stars that are part of bound clusters and the large-separation peak as arising from unbound stars that have dispersed from their natal environments. Based on this, we retain in our sample only those stellar pairs for which the separation between the stars is > 30 pc a time $\Delta t = 100$ Myr after the stars' birth. This criterion effectively limits our sample to pairs of

stars that are no longer recognisable as members of the same bound cluster in physical space.

We are now in a position to quantify the change in action differences between the pairs of stars that we retain. For a given pair of stars at each Δt , we define the absolute change in action difference for each component (J_R, J_ϕ, J_z) as the change in their action difference at age Δt from the action difference at the birth snapshot:

$$\delta_{\text{abs}}\Delta J(t, \Delta t) = \left| \left| J_i(t + \Delta t) - J_j(t + \Delta t) \right| - \left| J_i(t) - J_j(t) \right| \right| \quad (11)$$

where $J_i(t)$ is one of the components of action of the i th star at time t . Thus for example consider a pair of stars born at time t whose radial actions at this time are $J_{R,i}(t) = 2 \text{ km s}^{-1}$ kpc and $J_{R,j}(t) = 3 \text{ km s}^{-1}$ kpc, and at a time $\Delta t = 100$ Myr later we find that their actions are $J_{R,i}(t + \Delta t) = 1 \text{ km s}^{-1}$ kpc and $J_{R,j}(t + \Delta t) = 4 \text{ km s}^{-1}$ kpc. We would then say that $\delta_{\text{abs}}\Delta J_R(t, \Delta t) = 2 \text{ km s}^{-1}$ kpc for this stellar pair, since the separation in actions has grown from 1 km s^{-1} kpc at birth to 3 km s^{-1} kpc at 100 Myr after birth. We also define relative change in action difference as the absolute change in action difference divided by the geometric mean of the actions of the stars at the later time:

$$\delta_{\text{rel}}\Delta J(t, \Delta t) = \frac{\delta_{\text{abs}}\Delta J(t, \Delta t)}{\sqrt{J_i(t + \Delta t)J_j(t + \Delta t)}} \quad (12)$$

For our example stellar pair, we would have $\delta_{\text{rel}}\Delta J_R(t, \Delta t) = 1.5 \text{ km s}^{-1}$ kpc.

3 RESULTS

We are now prepared to characterise the evolution of action-space coherence for coeval stars. Our aim is to establish whether stars that are born together remain clustered in action space, and on what spatial and temporal scales this coherence persists. We begin by examining the overall behaviour of action differences of pairs as a function of their birth separation in Section 3.1. In Section 3.2, we distinguish how coherence differs across the three action components. Finally, we test whether the rate of decoherence depends on the Galactic environment by repeating the analysis in radial bins across the disc in Section 3.3.

3.1 Stars born together remain clustered in action space

As described in the previous section, for each of our 1 Myr snapshots, we identify pairs of stars born since the previous snapshot, and record their physical separation in the first snapshot at which we find them, d_{init} . We then track the actions of each star over time and calculate the absolute and relative changes in action differences for each stellar pair at each snapshot. We do this throughout the simulation, and the result is data set of stellar pairs at different times; each entry in this data set consists of the pair's distance at birth d_{init} , the time Δt since the pair was born, and the absolute and relative change in the pair's action difference since birth, $\delta_{\text{abs}}\Delta J_{R,z,\phi}$ and $\delta_{\text{rel}}\Delta J_{R,z,\phi}$. To study how these action changes depend on birth distance, we bin this data set by d_{init} , and for each time interval Δt in each d_{init} bin, we compute the median of the changes in action differences for all stellar pairs. We plot these median action differences for each component as a function of time in Figure 2 for absolute action changes, and in Figure 3 for relative changes.

From the figures, it is clear that the stars born close together show much smaller change in action differences over time compared to the ones born far apart. That is, we find that at any given Δt , the absolute and relative changes of all actions are much smaller for the small

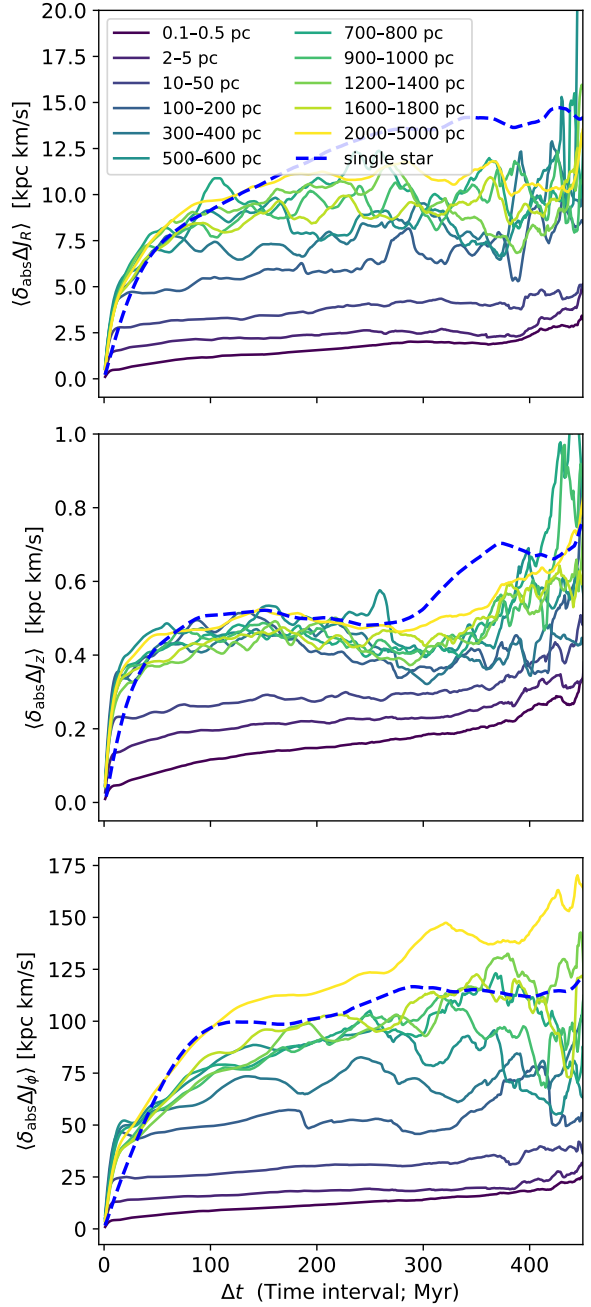


Figure 2. Median of absolute change in action difference (row-wise in order: $\delta_{\text{abs}}\Delta J_R$, $\delta_{\text{abs}}\Delta J_z$ and $\delta_{\text{abs}}\Delta J_\phi$) versus time for coeval pairs of stars binned by stellar separation at birth; birth distance bins are indicated by colour, as shown in the legend. For comparison, the blue dashed line shows the change in the action of *single* stars relative to their own initial actions as a function of age gap; this result is taken from from Paper I. As expected, for stars both at large separations (lighter-coloured solid lines) the actions change in essentially uncorrelated ways, so the changes in action between pairs of stars are similar to the changes for individual stars (blue dashed line), but stars born close together (darker solid lines) change their actions in correlated ways, and so the relative change in action for pairs of stars is much smaller than the change in actions for single stars.

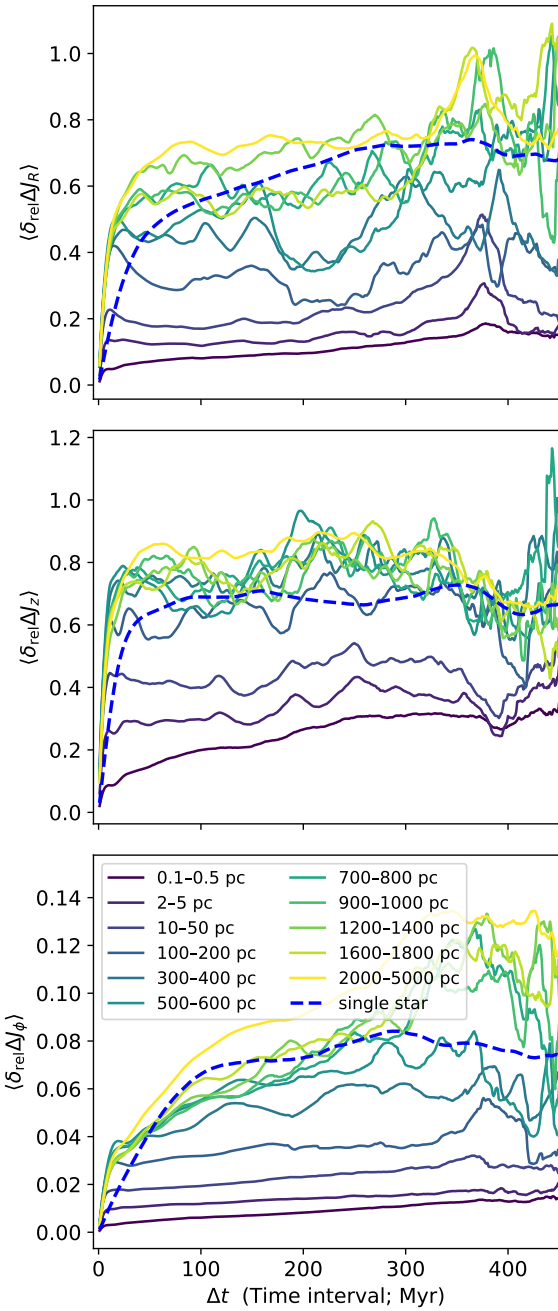


Figure 3. Same as Figure 2, but now showing changes in relative action $\delta_{\text{rel}}\Delta J_{R,z,\phi}$ rather than absolute action $\delta_{\text{abs}}\Delta J_{R,z,\phi}$.

d_{init} bins than for the larger ones. As the birth separation increases, the curves for different bins begin to converge (in both absolute and relative changes in the action differences), suggesting that the pairs of stars born sufficiently far apart evolve independently in action space, i.e. they are decoherent from birth.

To contextualise these changes, we also show the typical single-star action evolution from Paper I in Figure 2 and Figure 3 as the blue dashed lines. This quantity is defined as the change in the action of a single star relative to its initial action, so for example the blue dashed line in the top panel of Figure 2 indicates that, for the median star in the simulations, its radial action 150 Myr after birth will be ≈ 10 kpc

km/s different than it was at birth. The plot shows that the single-star action change with respect to itself in time closely matches the change in action difference for pairs of stars that are born far apart, confirming that these stars undergo uncorrelated evolution in action space. By contrast, pairs born close together retain coherence in action space over the entire ~ 0.5 Gyr timescale of our simulation. We emphasise that this does not mean that these stars' individual actions do not change – as the blue dashed line shows, their individual actions are in fact changing significantly. It is simply that for stars that were born close together in space, the changes in action they experience are very similar, so the change in the difference of actions between the two stars is much less than the action change each star undergoes individually. We can conceptualise this as the stars undergoing a random walk but doing so while holding hands: after a long enough time the two stars may both wind up very far from where they started, but they will still be close to each other. For the stars in the smallest bins of d_{init} , the relative action difference change remains well below 50% throughout the simulation (Figure 3). This establishes that stars born together remain together in action space over at least hundreds of millions of years, even as they drift apart physically.

3.2 Different components decohere on different spatial scales

A second quantity that we can read off from Figure 2 and Figure 3 is how closely together stellar pairs must be at birth for their actions to separate noticeably more slowly than the rates at which the actions of single stars drift – that is, for what values of d_{init} do we observe that the change in action separation for stellar pairs (solid lines) is significantly smaller than the rates at which individual stellar actions drift (dashed blue lines)? We can think of stars with d_{init} smaller than this value as coherent in action space, while those with larger d_{init} are incoherent. Interestingly, for radial and azimuthal actions, decoherence emerges gradually at birth separations on the scales of kiloparsecs. However, for vertical action, coherence is lost at much shorter distances of hundreds of parsecs.

This difference is physically significant. In Paper I, we argued that vertical actions and radial actions have different drivers of change: vertical actions are primarily influenced by local perturbations such as GMCs, while radial actions are affected by large-scale structures such as spiral arms. This picture is consistent with the spatial scales of decoherence that we find here: the vertical action decoheres over scales comparable to the vertical disc scale height (Bobylev & Bajkova 2021; Vieira et al. 2023), while radial and azimuthal actions decohere over much larger distances, reflecting the scale of spiral arm structure, which is comparable to the radial scale length of the stellar disc (Castro-Ginard et al. 2021; Bobylev & Bajkova 2021).

These results suggest that the coherence in action space is a function of birth distance but also depends on which action component is considered and what physical processes dominate its evolution. These dependencies provides quantitative constraints on how long and how far action clustering persists in each component of action. As we explore in Section 4, this can directly inform efforts to reconstruct disrupted stellar associations in the Milky Way by assessing the maximum allowable action difference as a function of birth separation and time since formation.

3.3 Radial Dependence

To test whether action decoherence depends on Galactic environment, we repeat our analysis in radial bins of 1 kpc. In Paper I, we found that the relative action change was faster and stronger in the inner disc compared to the outer disc, even after removing the expected

dependence due to radial variation of the galactic orbital period, as expected given the large number of perturbation drivers (e.g., higher density of GMCs) in the inner disc.

Here, however, we restrict ourselves to stars that are born close together. In Section 3.1, we saw that such stars remain clustered in action space throughout the simulation. For each radial bin, we select coeval stars with birth separations of $0.5 - 2$ pc and compute the median of relative change in action difference at each Δt ; results for other small d_{init} bins are qualitatively similar, so we show only the $0.5 - 2$ pc bin for clarity. The results are plotted in Figure 4 for all three components of action, for radial bins of 1 kpc spanning $2 - 19$ kpc (the range where actions are available). Beyond the noise especially at large Δt values (where only the earliest-born stars contribute, leading to small-number statistics), we find no clear radial dependence in the change of action difference. This is somewhat surprising, since one might expect faster divergence in the inner disc. However, it is important to note that we are measuring changes in action *differences*, not the actions themselves. Hence, the result implies that conatal stars (that are born within $0.5 - 2$ pc of each other) experience similar perturbations regardless of their locations in the Galaxy, and thus their actions remain clustered to a comparable extent in both the inner and outer disc.

4 APPLICATION TO OBSERVATIONS

Having established a framework to quantify the divergence of stellar actions of pairs of stars as a function of initial separation and time, we now aim to apply these results to observed moving groups and stellar streams in the Milky Way disc. The goal of this section is to test whether present-day kinematic substructures are consistent with the hypothesis that they are unbound descendants of initially compact star clusters (Lada & Lada 2003; Baumgardt & Kroupa 2007; Kuhn et al. 2019), and to place quantitative constraints on their initial sizes using our simulation library.

The key diagnostic used throughout this section is present-day distribution of pairwise action differences within each candidate stream. Under the simplifying hypothesis that a stream formed in a single, compact star-formation event, all members share nearly identical actions at birth (i.e. zero pairwise action difference). As the system evolves in the Galactic potential for time τ (the present-day age of the object), action differences should grow according to the behaviour characterised by our simulation. Thus, we can infer the range of plausible birth separations for members of the stream.

Firstly, in Section 4.1, we summarise the data sources used and their preparation. We describe the methodology we use to compare the observed distributions with the simulation predictions in Section 4.2. In Section 4.3, we present the results for the sample and discuss their implications. Section 4.4 talks about the completeness of observational membership and its effect on our analysis, while other caveats of the method are discussed in Section 4.5.

4.1 Data selection and preparation

Our observational sample is drawn from the catalogue complied by Hunt & Reffert (2024b), which classifies objects previously identified as open clusters into bound clusters and unbound moving groups based on their Jacobi radii. The associated catalogue (Hunt & Reffert 2024a) provides membership lists for all systems, along with per-member astrometry (RA, Dec, PMRA, PMDec, radial velocity and its uncertainty) from *Gaia* DR3 (Gaia Collaboration et al. 2023) as well as cluster-level parameters such as age percentiles (16th,

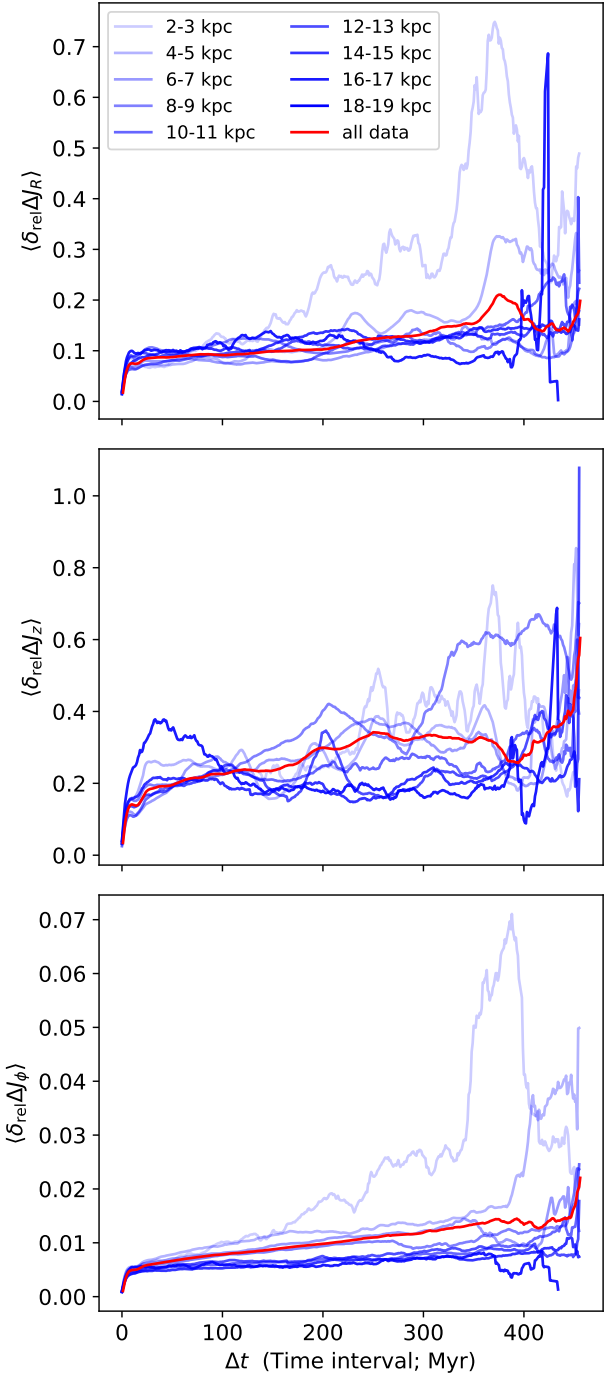


Figure 4. Median of relative change in action difference (row-wise in order: $\delta_{\text{rel}}\Delta J_R$, $\delta_{\text{rel}}\Delta J_z$ and $\delta_{\text{rel}}\Delta J_\phi$ in order) for coeval pairs of stars in time with their birth distances in the $0.5 - 2$ pc bin. The darker blues represent higher radii. The red curve shows the median of the relative change in action differences for the entire dataset of pairs of coeval stars born within $0.5 - 2$ pc of each other.

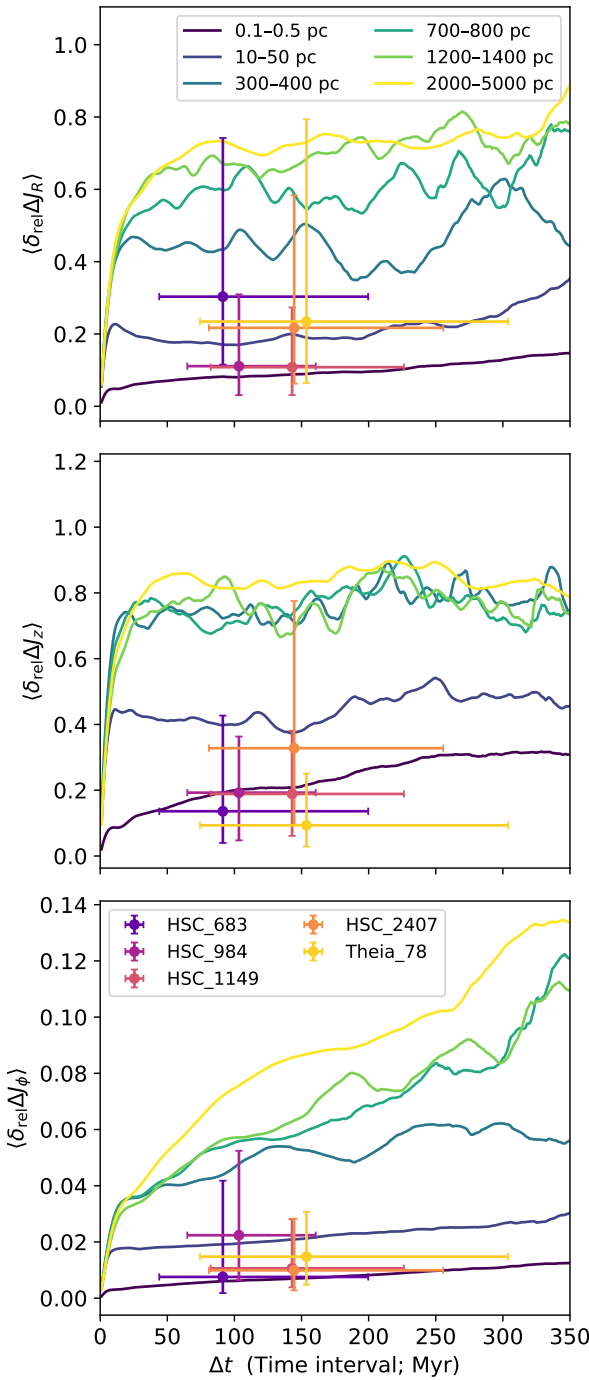


Figure 5. Relative action differences calculated for some of the observed moving groups (markers) placed on the theoretical grid of action-space evolution (coloured lines indicating different birth distance bins as shown in the legend). Rows from top to bottom show $\delta_{\text{rel}}\Delta J_{R,z,\phi}$, respectively. Each point represents the median of the distribution $\{\delta\Delta J_{\text{obs}}\}$ and age of a moving group, with error bars showing the 16th and 84th percentiles. The lines are identical to those shown in Figure 3, though we show only a subset here to minimise clutter.

50th and 84th) and current radius of the object in parsecs. We note here that Hunt & Reffert (2024b) do not consider radial velocities in their membership determination method. Hence, some stars with discrepant radial velocities may be miscategorised as members. To assess the robustness of our results to this effect, we repeated our entire analysis after excluding members that deviate by more than 3σ in radial velocity from the group mean. This test, presented in the Appendix A, yields similar results.

For all the members of each candidate moving group, we need to assemble their six-dimensional phase-space information for the computation of stellar actions. We adopt RA, Dec, proper motions and radial velocities directly from the membership list in the Hunt & Reffert (2024a). When the catalogue does not provide a radial velocity, we supplement it using large spectroscopic surveys: GALAH DR4 (Buder et al. 2025), APOGEE DR17 (Abdurro'uf et al. 2022) and RAVE DR6 (Steinmetz et al. 2020), selecting the measurement with the smallest quoted uncertainty when multiple values are available. Distances are taken from the probabilistic parallax-based estimates of Bailer-Jones et al. (2021). For a small fraction of stars lacking an individual distance estimate, we assign the mean distance of the remaining members of the group as an approximation. This substitution is rare, since radial velocities are more often missing than distances, and stars without reliable velocities are removed from the sample altogether because accurate 6D phase-space information is essential for action computation.

To ensure robust statistics for pairwise comparisons, we retain only those moving groups with at least ten member stars possessing full 6D information. This guards against unstable inference for poorly sampled systems. We also limit the sample to the parameter space covered by our simulations: objects are required to have an 84th percentile age less than 456 Myr, corresponding to the maximum Δt in our simulated library. When the published age uncertainty is large, we retain the object provided that a significant portion of its age posterior lies within this range.

The actions of the member stars are calculated using the Stäckel approximation (Binney 2012) implemented in the galpy package (Bovy 2015). Since we have the 6D astrometry of the stars, we can directly integrate each star's orbit in a Milky Way potential which is taken to be the commonly-used MWPotential2014 (Bovy 2015) in our case. We integrate the orbits in this potential for 50 internal time units (corresponding to ≈ 1.9 Gyr) and use the resulting orbit to estimate the local focal parameter Δ via the `estimateDeltaStaeckel` function. Given the potential and Δ , we compute the actions using `actionAngleStaeckel`¹.

For each moving group, we then take all possible pairs of stars and evaluate their relative change in action difference using equation 12 under the assumption that their initial action difference is zero, i.e. $|J_i(t) - J_j(t)| = 0$. Hence, for each stream, we get a distribution of observed relative action changes, represented by $\{\delta\Delta J_{\text{obs}}\}$, which characterises the present-day kinematic coherence of the stream. These values are upper limits, since if the initial action distances were non-zero then the value $\{\delta\Delta J_{\text{obs}}\}$ would be smaller.

Using the distribution $\{\delta\Delta J_{\text{obs}}\}$ and the system's age (and uncertainty), we can directly place each observed stream on the theoretical map of action-space coherence evolution shown in Figure 3. Figure 5

¹ We note that our simulation action predictions were computed using the epicyclic approximation described in Section 2.2. However, tests in Paper I indicate that the epicyclic approximation and direct action computation produce comparable trends for the disc populations we consider (within $\sim 22\%$ for radial and $\sim 10\%$ for vertical action).

illustrates this comparison: coloured lines, as before, indicate the median of change in action difference with respect to time for coeval pairs of stars binned by stellar separation at birth. We then overplot a randomly-chosen subset of the observed moving groups as points, with the medians of their distribution $\{\delta\Delta J_{\text{obs}}\}$ on the vertical axis and median age on the horizontal axis; the error bars represent the 16th – 84th percentile ranges in both quantities. The relative position of a moving group point with respect to the lines of different stellar birth separation provides an estimate of the upper limit on its initial size – the effective ‘birth radius’ of the cluster that may have evolved into the present-day observed stream.

This qualitative comparison can be done for all the three components of action. However, visual inspection of Figure 5 shows that the vertical action yields the most stringent constraints on initial size. This is expected since, as seen in Section 3.2, vertical action differences decorrelate over smaller physical scales than the azimuthal or radial components. Therefore, in the following sections, where we develop a quantitative, probabilistic inference framework for estimating initial cluster sizes, we restrict our analysis to the vertical action component.

4.2 Methodology

Our goal is to estimate the most likely initial separation (d_{init}) of stars that make up present-day stellar streams by comparing their observed distribution of action differences to the simulation-based probability distributions of relative action difference changes, while marginalising over the uncertainty in the streams’ age.

To explain our approach, we begin with the simplified case where we know the stream’s age τ exactly, before generalising to the situation where τ is uncertain. Our first step for the simplified case is to construct the distribution of predicted action differences as a function of d_{init} for stars of this age based on our simulations. We therefore select all the stellar pairs whose age Δt is equal to the stream age τ , giving us a sample of pairs that are each characterized by an initial separation d_{init} and an increase in relative vertical action difference $\delta_{\text{rel}}\Delta J_{z,\text{sim}}$. We next select a random sample of 2 million pairs from the remaining data; we use 2 million rather than all the pairs ($\sim 10^8$ samples total for smaller values of Δt , diminishing for larger Δt) to keep the computational cost tractable. From these 2 million pairs, we construct a kernel density estimate (KDE) in the two variables $a \equiv \log d_{\text{init}}$ and $x_{\text{sim}} = \log \delta_{\text{rel}}\Delta J_{z,\text{sim}}$, using Silverman’s rule to set the bandwidth of the KDE. We denote the resulting KDE in the two variables $\mathcal{P}_{2D}(x_{\text{sim}}, a | \tau)$. We next reduce this to a series of 1D marginal KDEs for x_{sim} at each a by evaluating

$$\mathcal{P}_{1D}(x | a, \tau) = \frac{\mathcal{P}_{2D}(x_{\text{sim}}, a | \tau)}{\int_{-\infty}^{\infty} \mathcal{P}_{2D}(x_{\text{sim}}, a | \tau) dx_{\text{sim}}}. \quad (13)$$

In practice we compute this integral by evaluating the KDE on a 2D grid covering the full range of a and x_{sim} . After that, we extract slices at constant a , normalising the distribution at each a to ensure that the total probability integrated over x_{sim} sums to 1 for each a ; this normalization step corresponds to the denominator of equation 13. Finally, we construct an interpolating function for each value of a . The result is a function $\mathcal{P}_{1D}(x | a, \tau)$ that lets us efficiently predict the probability density function (PDF) of action differences x we expect for a population born with a particular initial size a and a present-day age τ .

The top panel of Figure 6 shows examples of cumulative probability distribution functions (CDFs) corresponding to the PDFs $\mathcal{P}_{1D}(x | a, \tau)$ for different a values and at an age $\tau = 148$ Myr, chosen to correspond to the central age estimate for an example

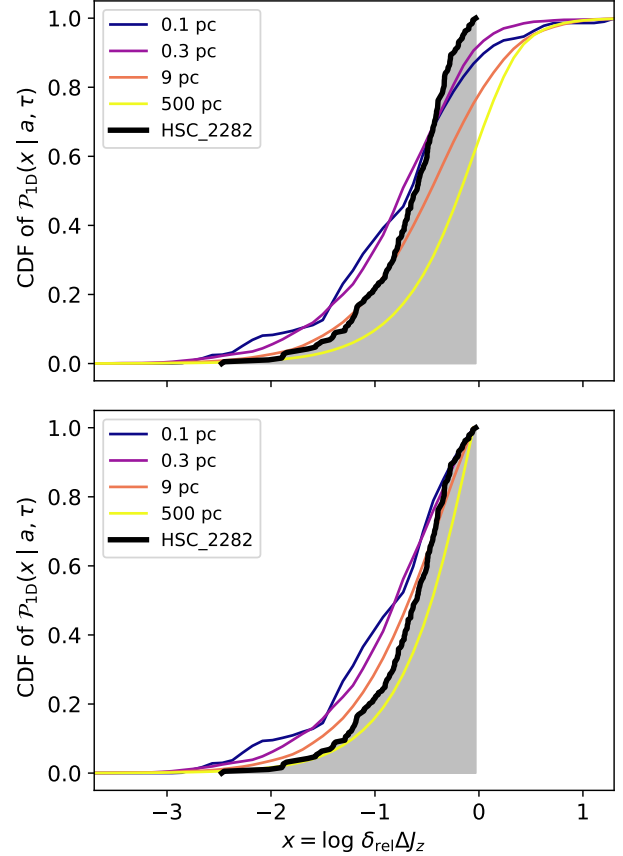


Figure 6. Coloured lines show examples of cumulative distributions corresponding to the one-dimensional probability distributions, $\mathcal{P}_{1D}(x | a, \tau)$, of log vertical action difference $x = \log \delta_{\text{rel}}\Delta J_z$, for different initial separations d_{init} (as indicated in the legend) and stellar populations of age $\tau = 148$ Myr. The top and bottom panels show results for the full and truncated distributions, respectively – see main text for details. The black solid line with shading shows the cumulative distribution for observed stellar pairs in the example stream HSC 2282 for comparison.

stream, HSC 2282. The thick black line represents the CDF of log action differences $\{x_i\}$ for the observed members of the stream, while coloured lines represent predictions constructed from our simulations for different initial separations, as indicated in the legend. Notably, the observed CDF appears truncated near $x \sim 0$, and this behaviour is consistent across all streams we examined in our dataset, which suggests it could be an observational artefact: if stream members are too far away in action space (and, correspondingly, in physical space), they become increasingly unlikely to be observed or classified as stream members in the catalogue. To account for the possible effects of this observational limitation, we consider a modified method for constructing our theoretical PDFs $\mathcal{P}_{1D}(x | a, \tau)$ under the assumption that the lack of observed pairs at high $\delta_{\text{rel}}\Delta J_z$ is primarily a result of observational incompleteness, in which case we must apply a similar truncation to the theoretical predictions. We therefore construct a modified version of $\mathcal{P}_{1D}(x | a, \tau)$, which we denote $\mathcal{P}_{1D,\text{trunc}}(x | a, \tau)$, by setting $\mathcal{P}_{1D}(x | a, \tau) = 0$ for $x > x_{\text{max,obs}}$ where $x_{\text{max,obs}}$ is the maximum observed value of $\log \delta_{\text{rel}}\Delta J_z$ for a given stream, and renormalising the value of $\mathcal{P}_{1D}(x | a, \tau)$ at $x < x_{\text{max,obs}}$ so that the integral over all x remains unity. We plot the

CDF corresponding to this truncated distribution in the bottom panel of Figure 6. In what follows we will carry out our remaining analysis using both the truncated and non-truncated versions of $\mathcal{P}_{1D}(x | a, \tau)$, since reality likely lies somewhere between the extreme assumptions that there are no observational biases against finding stream members with large action difference (corresponding to the top panel in Figure 6) and that any disagreement between the observations and the predictions at high x is solely due to observational bias (the lower panel).

Examining either panel of Figure 6, it is clear that we can pick out by eye which values of d_{init} yield predict CDFs of action differences that are similar to the observed one. To render this intuition quantitative, we compute the likelihood of observing the action difference distribution $\{x_i\}$ given a particular pair of values (a, τ) as the product of individual probability for each observation:

$$\mathcal{L}(\{x_i\} | a, \tau) = \prod_i \mathcal{P}_{1D}(x_i | a, \tau) \quad (14)$$

where $\mathcal{P}_{1D}(x | a, \tau)$ is the 1D PDF computed either for all the simulation data or for the truncated version. If we adopt a flat prior in $a = \log d_{\text{init}}$, the posterior probability distribution for a then follows directly from the likelihood:

$$\mathcal{P}_{\text{post}}(a | \{x_i\}, \tau) \propto \mathcal{L}(\{x_i\} | a, \tau) \quad (15)$$

This posterior describes the probability distribution for log initial size $a = \log d_{\text{init}}$ at a fixed age τ .

Now we can relax the assumption of known, fixed stream age τ . Instead, we assume that the age is described by a Gaussian distribution with mean μ (the median age reported in the catalogue) and standard deviation σ (derived from the 16th and 84th percentile ages assuming a normal distribution). To incorporate this observational uncertainty, we marginalise over τ by taking our final posterior PDF of a to be

$$\mathcal{P}(a | \{x_i\}, \mu, \sigma) = \int \mathcal{L}(\{x_i\} | a, \tau) \mathcal{P}(\tau | \mu, \sigma) d\tau, \quad (16)$$

where $\mathcal{P}(\tau | \mu, \sigma)$ is a Gaussian distribution with mean μ and dispersion σ . In practice, we perform this age marginalisation by drawing $\sim 10^4$ samples from the age distribution of the stream and evaluating conditional likelihood at each sampled age τ using equation 14. Then, the likelihoods are averaged over the ensemble to obtain the age-marginalised posterior given by equation 16. Again, we carry out this procedure for both the truncated and non-truncated versions of \mathcal{P}_{1D} . For numerical stability, we restrict the sampled ages to $\tau \lesssim 397$ Myr, since at later times the number of simulation pairs falls below 2×10^6 , leading to noisy statistics as seen in Section 3. From the final posterior probability distribution $\mathcal{P}(a | \{x_i\}, \mu, \sigma)$, we report the median ($d_{\text{init}50}$), 84th ($d_{\text{init}84}$), and 97.5th ($d_{\text{init}97}$) percentile, which provide a median estimate and upper confidence limits on d_{init} .² We show the CDF corresponding to the posterior for our example stream HSC 2282 in Figure 7.

Finally, to quantify how well the simulation and observed distributions agree, we compute the L^1 distance between them at each age sampled:

$$L^1(\tau) = \frac{1}{2} \int |\mathcal{P}_{\text{post}}(x | a_{\text{ml}}, \tau) - \mathcal{P}_{\text{obs}}(x)| dx \quad (17)$$

² We do not report lower percentiles because, to remind readers, the values we obtain are always upper limits because they are derived under the assumption of negligible action separation at birth; any finite difference in the actions of stream members at birth would yield lower estimates of d_{init} .

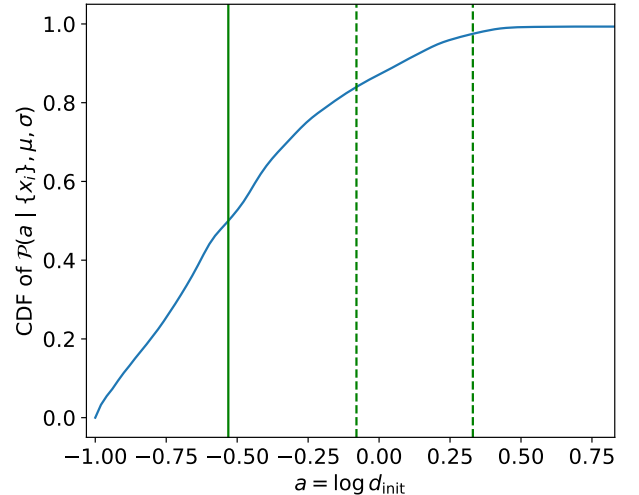


Figure 7. Cumulative distribution corresponding to the marginal posterior distribution, $\mathcal{P}(a | \{x_i\}, \mu, \sigma)$, for HSC 2282, given its observed action differences $\{x_i\}$, age $\mu = 148.17$ Myr and $\sigma = 125.64$ Myr. This CDF is derived for the non-truncated assumption (see main text). The median logarithmic initial size $a_{50} = \log d_{\text{init}50}$ (in units of pc) is shown as the solid green vertical line while the 84th and 97th percentile upper limits $a_{84} = \log d_{\text{init}84}$ and $a_{97} = \log d_{\text{init}97}$ are shown as the two dashed green vertical lines to its right.

where a_{ml} is the maximum-likelihood estimate of $a = \log d_{\text{init}}$. The factor of $1/2$ ensures that $L^1(\tau)$ ranges from 0 for identical distributions to 1 for completely non-overlapping ones. The final, age-marginalised value of L^1 for the stream is then:

$$L_f^1 = \int L^1(\tau) \mathcal{P}(\tau | \mu, \sigma) d\tau \quad (18)$$

This L_f^1 serves as a global diagnostic of how well the simulated distribution and its best fitting d_{init} reproduces the observed one, with lower values correspond to better agreement. As usual, we compute this diagnostic both using the full simulation data set and the version where we assume that the high $\delta_{\text{rel}}\Delta J_z$ tail is truncated by observational selection effects.

4.3 Results and discussion

Figure 8 presents the distribution of inferred median initial sizes (a_{50}) for all the streams in our sample. The top panel shows the values obtained from the full posterior probability distribution that corresponds to assuming no observational incompleteness, while the bottom panel shows the results derived from the truncated version of the distribution that corresponds to assuming that all high $\delta_{\text{rel}}\Delta J_z$ stars have been missed. Figure 9 displays the distribution of the corresponding L_f^1 and $L_{f,\text{trunc}}^1$ values for all streams, which quantify the quality of the fit – smaller values indicate better agreement between the observed and modelled action-difference distributions. Most streams exhibit $L^1 \lesssim 0.2$, though the distribution shows a mild tail toward poorer fits (still < 0.5). We mark the 90th percentiles of the two distributions with vertical black lines (solid for L_f^1 and dashed for $L_{f,\text{trunc}}^1$), which effectively delineate the tail region. Streams to the left of this line are considered well-fit by our model. The filled histograms in the top and bottom panels of Figure 8 show the median initial size distributions for these “well-fit” streams, while the

Cluster Name	Median age [Myr]	Present size [pc]	$d_{\text{init}50}$ [pc]	$d_{\text{init}84}$ [pc]	$d_{\text{init}97}$ [pc]	L_f^1	$d_{\text{trunc}50}$ [pc]	$d_{\text{trunc}84}$ [pc]	$d_{\text{trunc}97}$ [pc]	$L_{f,\text{trunc}}^1$	f_{comp}
ASCC_100	64.89	21.17	0.28	0.42	0.65	0.19	0.38	0.70	1.42	0.16	0.91
ASCC_104	121.70	32.19	476.77	871.23	983.36	0.16	493.33	885.88	985.08	0.18	0.98
ASCC_18	9.26	16.17	0.45	0.62	3.21	0.09	0.63	0.85	3.24	0.10	0.95
ASCC_33	215.38	21.42	0.31	0.73	1.86	0.17	0.83	2.97	14.56	0.14	0.85
ASCC_69	72.90	26.99	0.25	0.48	0.99	0.15	0.92	2.92	13.87	0.11	0.82
ASCC_73	158.29	38.93	0.32	1.34	2.83	0.18	29.21	49.36	73.43	0.08	0.85
Alessi-Teutsch_4	132.97	28.06	0.20	0.35	0.62	0.32	0.48	1.20	3.11	0.16	0.67
Alessi_13	24.75	42.07	659.41	819.64	983.16	0.06	666.91	879.90	989.71	0.06	0.99
Alessi_145	168.03	82.18	0.30	0.45	0.74	0.27	0.53	0.94	1.71	0.14	0.84
Alessi_84	117.08	27.70	0.42	0.74	1.45	0.14	0.48	0.88	1.57	0.15	0.99

Table 1. Summary of inferred parameters for the first 10 streams (alphabetically) in our sample. Columns list the stream name, median stellar age (in Myr), present-day physical size (in pc), inferred initial size percentiles from both the full and truncated posterior distributions (all in pc), associated L^1 norms quantifying the fit quality, and the completeness fraction f_{comp} . The stream name, median stellar age and present-day physical size are taken from Hunt & Reffert (2024a). The full table is provided in machine-readable format (check Data Availability).

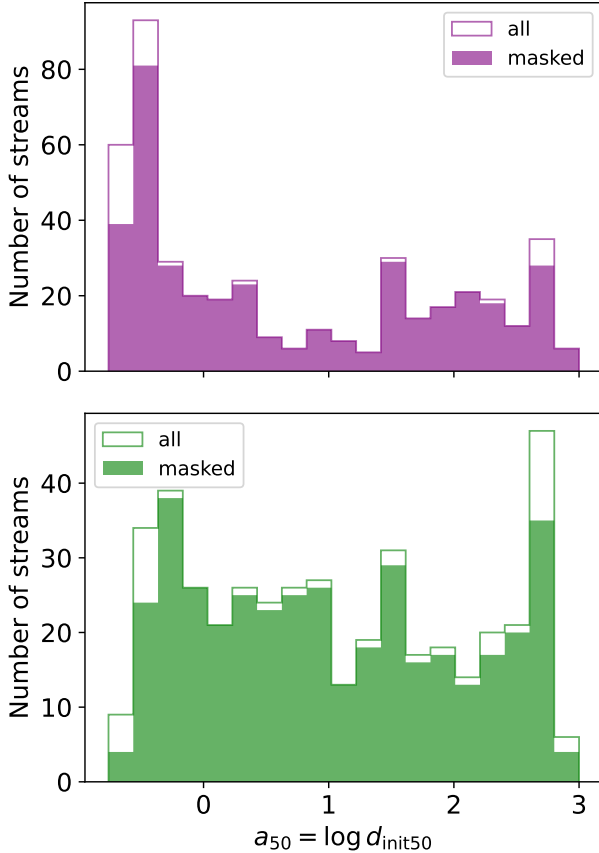


Figure 8. Distribution of the inferred median logarithmic initial sizes (a_{50} , in units of pc) for all streams in our sample. The shaded histogram highlights the subset of “well-fit” streams, selected by applying a cut on their L_f^1 values. The top panel shows results derived from the full posterior probability distribution, $\mathcal{P}(a \mid \{x_i\}, \mu, \sigma)$, which is the appropriate distribution if the observed samples are complete, while the bottom panel shows those obtained from the truncated posterior distribution, which corresponds to the assumption that the observational samples are systematically missing stream members with large action differences.

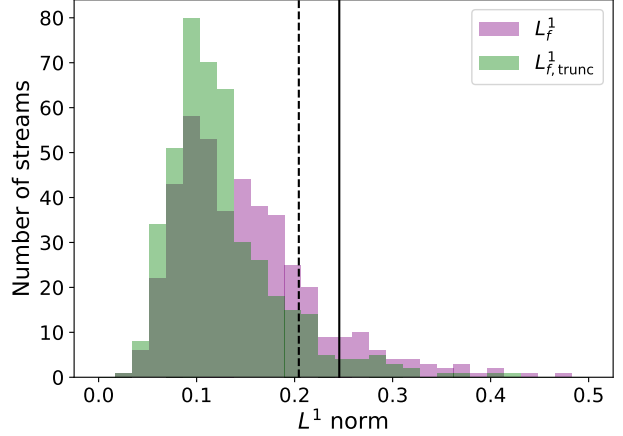


Figure 9. Distribution of the L_f^1 (purple) and $L_{f,\text{trunc}}^1$ (green) values that characterise how well the observed distribution of action differences matches the best-fitting simulation-predicted distribution. The black solid line represents the 90th percentile of L_f^1 while the dashed line shows the same for $L_{f,\text{trunc}}^1$.

unfilled histograms show the results if we do not omit these less well-fit streams; the overall shape of the distribution remains largely unchanged after this quality cut. To illustrate the associated uncertainties in the inferred sizes, Figure 10 shows the CDFs of median initial size (a_{50}) along with the 84th and 97.5th percentile initial size (a_{84}, a_{97}) for the entire sample.

All derived quantities – including the median, 84th, and 97.5th percentiles of inferred initial sizes, corresponding L_f^1 statistics (for both the full and truncated probability distributions), stream name, and its median stellar age – are compiled in Table 1. We also provide an estimated completeness fraction, f_{comp} , of each stream’s membership under the hypothesis that high action difference stream members have been missed – see Section 4.4 for full details of how we compute this quantity. The complete table is available in a machine-readable format as supplementary material.

Examining the distribution of the inferred initial sizes in Figure 8, we find that the streams span more than three orders of magnitude in $d_{\text{init}50}$. We note that these streams have an average present size

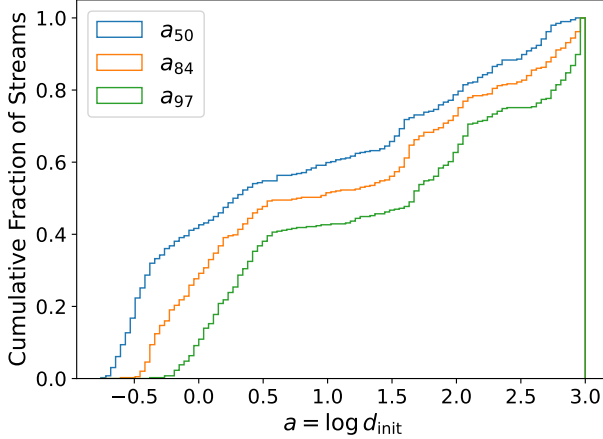


Figure 10. Cumulative distributions of the inferred logarithmic initial sizes (median a_{50} , 84th percentile a_{84} and 97.5th percentile a_{97}) for the “well-fit” streams in our sample represented by the colours specified in the legend.

of ~ 30 pc. The fact that most inferred birth sizes are tens to hundreds of times smaller suggests that a large fraction of these systems were compact stellar clusters that have since become unbound and dispersed along their orbits. We interpret the left side of the distribution, where $d_{\text{init}50} \lesssim 3$ pc, as representing these compactly born objects, whose members have gradually phase-mixed to produce the extended kinematic streams observed today. In contrast, the right side of the distribution contains objects with inferred initial sizes of several hundreds to thousands of parsecs, comparable to or larger than their current size. Such systems could not plausibly have been bound clusters in the past. Instead, we propose that these groups were formed through resonant processes, in which stars are trapped or aligned in action space by non-axisymmetric perturbation in the Galactic potential. These mechanisms have been associated with spiral arms and bar resonances (e.g., Sellwood 2010; Khoperskov et al. 2020; Trick et al. 2021; Palicio et al. 2023), which can generate coherent moving groups without a common birth origin (De Leo et al. 2025). The action difference distributions of these systems resemble those of randomly selected stars in our simulation (where correlations in action differences have already decohered; see Figure 2), consistent with a non-coeval, resonance-driven origin. Another possibility is that some of these groups with large initial birth size consist of stars that formed in the same large-scale complex, leading to an intrinsic spread in birth actions that mimics a coherent kinematic substructure at the present day.

In order to demonstrate that our analysis method is picking up on real differences in stellar properties when assigning some streams small d_{init} and others much larger values, in Figure 11 we provide a representative comparison between the observed action-difference distributions for two stream cases: Theia 323, with inferred birth size of 0.3 pc, and HSC 1964, which has an inferred birth size of 363.4 pc. It is clear from the figure that Theia 323 shows visibly lower pair-wise action differences than HSC 1964. This validates our Bayesian inference framework, demonstrating that it is capturing real variations in the action-space coherence of stellar groups.

We further examine whether the inferred initial sizes depend systematically on the age of the stream. In Figure 12, we plot the joint distribution of $a_{50} = \log d_{\text{init}}$ and median stellar age for each stream, using age estimates from the Hunt & Reffert (2024a) catalogue. We

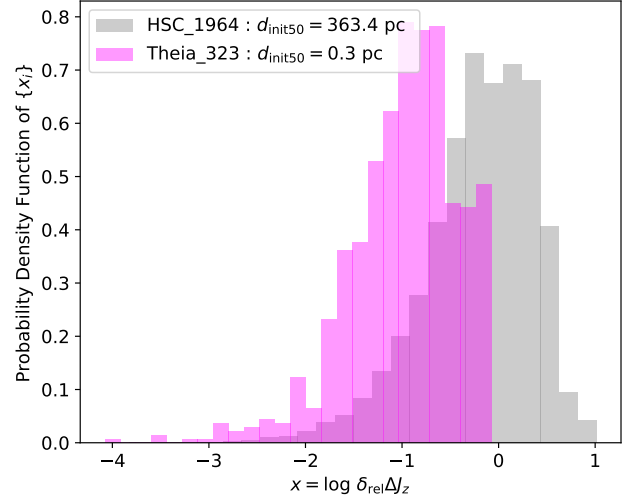


Figure 11. The observed pairwise action differences logarithm $\{x_i\}$ distribution for two representative streams: (i) Theia 323 (in pink) with inferred initial size $d_{\text{init}50} = 0.3$ pc, indicative of a compact origin stream; and (ii) HSC 1964 (in grey) with inferred initial size $d_{\text{init}50} = 363.4$ pc, representative of a resonant structure.

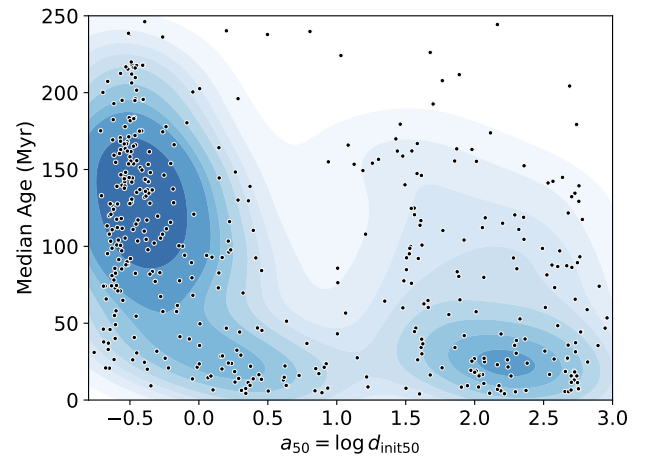


Figure 12. Distribution of the inferred median logarithmic initial sizes (a_{50}) for all streams in our sample, plotted as a function of their median stellar ages (black points). Blue contours indicate regions of higher density in the (a_{50}, age) plane, highlighting the overall structure of the distribution.

find that streams identified as disrupting clusters (those lying to the left of the figure) span the full age range of our sample, with no obvious bias to young or old age. Those with large inferred initial separations based on their action difference distribution are mildly biased to younger ages, but not by a very significant amount.

4.4 Completeness of the data

If we adopt the hypothesis that the distribution of action differences $\delta_{\text{rel}}\Delta J_z$ is truncated at the high end because the stream membership lists are incomplete, we can use the comparison between the observed distributions and our best-fitting models to estimate what

fraction of stream members have been missed. We quantify this by for each stream defining the completeness fraction, f_{comp} , which we compute by comparing the CDF of observed action differences for the stream members with that of a non-truncated probability distribution $\mathcal{P}_{\text{ID}}(x | a, \tau)$, which represents the expected distribution in the absence of incompleteness/truncation. Here we take $x = \max(x_i)$ – the logarithm of largest observed action difference, and $a = d_{\text{trunc50}}$ – the inferred initial size of the stream assuming truncation. The key idea is that the non-truncated probability distribution derived from our simulation data, $\mathcal{P}_{\text{ID}}(x | a, \tau)$, is considered the “true” action difference distribution. However, due to incompleteness in observational data, we can not directly observe this distribution. Instead, we use the truncated model to estimate the best-fit initial size, d_{trunc50} , and use this to assess how the true action difference distribution should appear. By comparing this theoretical, non-truncated distribution to the observed distribution, we can determine the fraction of stream members that are likely missing. For example, in the case of HSC 2282, the best-fit initial size is found to be $d_{\text{trunc50}} \approx 9$ pc. As shown in the upper panel of Figure 6, the observed CDF reaches $\approx 75\%$ of the model CDF for $d_{\text{trunc50}} = 9$ pc (orange curve). This implies that the stream membership is about 75% complete, with the remaining 25% of members likely missing from the current catalogue. We emphasise that this is likely an upper limit on the true level of incompleteness, and a lower limit on the completeness, since it is derived under the assumption that *all* of the discrepancy between observed and modelled action differences at high $\delta_{\text{rel}}\Delta J_z$ is due to incompleteness.

We show the distribution of the completeness fractions for all streams calculated using this approach in Figure 13. The blue histogram represents f_{comp} for all the streams in our sample. However, it may not be meaningful to assess the ‘completeness’ of resonant structures (streams with large inferred initial sizes), since they most likely do not share a common origin. To address this, we also show the f_{comp} distribution for streams with inferred sizes $d_{\text{trunc50}} < 10$ pc, which are likely to have been compact clusters in the past. The distribution for this subset of streams is shown in pink in the figure. We find that only a small fraction of members are missing. The median f_{comp} for all streams is 0.93, and for streams with $d_{\text{trunc50}} < 10$ pc, it is 0.91. Thus, about 10% of the stream members are likely missing on average, with these missing members most likely concentrated in the high-tail end of the action difference distribution.

While this analysis suggests that incompleteness is modest, its effects are significant. Comparison between the top and bottom panels of Figure 8 highlights how missing data can significantly affect the inferred size distribution of the streams. In the non-truncated case (top panel), we assume that none of the members are missing and that there is no high-tail end in the observed action differences. This results in most streams having small inferred initial sizes. However, when we account for the possibility that the observational membership is incomplete and truncate our simulation model distribution at the highest observed action difference value, we obtain systematically larger initial sizes, as shown in the bottom panel. The non-negligible difference in the distributions demonstrates that the presence or absence of the high-action-difference tail can have a significant effect on the inferred initial size. If these members exist but are not detected, the true birth size of the stream must be larger to account for the missing high-action-difference tail.

This implies that if we wish to improve our ability to differentiate between resonance-induced streams and those that represent dispersion clusters, it is critical to improve, or at least better characterise, the completeness of stream membership lists. The improvement is most needed for high-action-difference stars whose kinematic properties

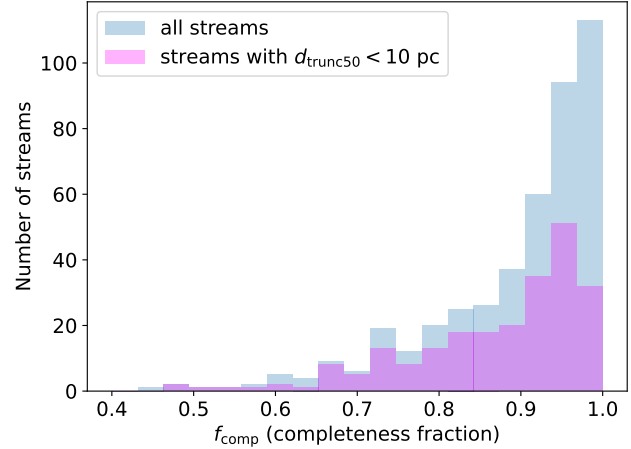


Figure 13. Distribution of the completeness fraction (f_{comp}) for all streams shown in blue. The pink histogram shows the same only for streams whose inferred initial size $d_{\text{trunc50}} < 10$ pc so they likely began as compact clusters instead of the probable resonant structures. This separation is useful to explore whether the streams that are more likely to have formed as compact clusters exhibit different completeness characteristics.

may place them at the edges of the observed action-space distribution, potentially leading to their exclusion from stream catalogues. One possible approach to this problem would be to expand the search in chemical space, by using the chemical properties of stars such as elemental abundances to identify stream members. The use of chemical abundances in addition to kinematic data is becoming increasingly feasible with large, high-resolution spectroscopic surveys like the APOGEE survey (Abdurro'uf et al. 2022), and GALAH (Buder et al. 2025) which provide precise elemental abundances for stars across the Milky Way. By combining both action and chemical space, we may be able to identify members that would otherwise be missed in a search based solely on position and kinematic information.

4.5 Caveats

Several caveats must be considered when interpreting these results. First, since we specifically chose ‘unbound’ stars in the simulation analysis, our results are based on the assumption that all stream members have been unbound for their entire lifetime. While the Hunt & Reffert (2024a) catalogue classifies these groups as ‘moving groups’ (and unbound) based on their Jacobi radii, many would have been bound in the past for a fraction of their age. Strictly speaking, the relevant age for our model would then be the time since they became unbound. However, given the large uncertainties in age estimates (typically $\gtrsim 30\%$), this distinction has limited practical impact.

Second, the inference framework assumes that our simulation library is based in the relevant range of the Galactic environment in which the streams we are applying it to have been. The simulation samples the full Galactic disc, providing a population-averaged model. Consequently, applying these results to a specific Galactic region requires caution. Young clusters residing in highly perturbed environment (e.g., near the bar, or in a tidally disrupted area) may experience stronger diffusion than is implied by our global calibration. However, older systems, which have orbited the Galaxy multiple times and sampled diverse environments, are expected to be better represented by our population-averaged model.

Finally, the reliability of our inferred quantities ultimately depends on the accuracy of stream membership, radial velocity measurements (which are often absent or have large uncertainties), the adopted Galactic potential model, and the approximations involved in the computation of actions. The improved astrometry and increased availability of radial velocity in the upcoming *Gaia* DR4 will mitigate some of these limitations. A more comprehensive, error-inclusive analysis that propagates the observational uncertainties is planned for future work.

It is also important to re-emphasise that our inferred initial size estimates represent upper limits. The model assumes that the group members were initially co-located in action space (i.e. had negligible initial ΔJ). If the true birth action spread were non-zero, a more compact initial configuration would be required to reproduce the same observed action differences in the present. In addition, as mentioned in Section 2.1, we may be overestimating the rate of action decoherence due to the resolution of our simulation's star particles. This, too, biases our inferred initial sizes towards an upper limit.

Overall, our findings support a dichotomy in the nearby kinematic substructures: (i) disrupted star clusters that have evolved into coherent stellar streams, and (ii) resonant or dynamically induced moving groups with no common formation origin. This method provides a new pathway to constrain the origins of streams, complementing chemical tagging and orbit integration approaches, and lays the groundwork for systematic application to the growing catalogue of streams uncovered by *Gaia*.

5 CONCLUSIONS

In this paper, we use high-resolution MHD simulation of a Milky Way-like galaxy to examine how stars that form together evolve in action space within a fully self-consistent environment that includes gas dynamics, star formation, and a live stellar disc with flocculent spiral arms. The main outcomes of our study are as follows:

- Stars born in close proximity to each other maintain strongly correlated actions throughout the ~ 0.5 Gyr period of our simulation. Their action differences show much smaller change than those of stars born farther apart, remaining well below 50% in relative change. In contrast, pairs separated by larger distances at birth show uncorrelated evolution, consistent with the stochastic diffusion seen for individual stars.
- The spatial scale over which co-natal stars lose correlation in action space varies by action component. Vertical action coherence breaks down over several hundred parsecs, while radial and azimuthal components become decorrelated only on kiloparsec scales. These differences reflect the dominant physical drivers of action evolution: vertical actions are perturbed by local structures such as GMCs (vertical disc scale height is of the order of hundred parsecs), while radial and azimuthal actions are shaped by large-scale non-axisymmetric features such as spiral arms which operate on kiloparsec scales.
- We find no significant dependence of the degree of action-space coherence on Galactocentric radius. Stars born close together in both the inner and outer disc experience similar levels of correlated perturbation, implying that different processes perturb their actions collectively rather than differentially i.e. they are moving together in logarithmic action space rather than being spread apart.
- We construct a probabilistic inference framework that links the present-day action distributions of stellar streams to their birth scales, using the library of action-difference evolution from the simulation. This allows the typical initial size of a stream to be estimated from

its observed phase-space structure and age. Applying this framework to the [Hunt & Reffert \(2024b\)](#) catalogue, we derive initial size estimates for 438 moving groups and quantify their fit quality and membership completeness. We provide these results as a resource for the community.

- The inferred birth sizes suggest a dichotomy among the streams. Most systems likely were in the past compact clusters that have since dispersed into streams, while others appear too extended to have been bound and are better explained by resonant or dynamically induced structures – possibly linked to the Galactic bar, spiral arms, or large star-forming complexes – rather than by common birth origin.

Together, these results establish the characteristic spatial and temporal scales over which co-natal stars lose dynamical coherence in the realistic Galactic environment of our high-resolution MHD simulation. By explicitly connecting present-day action-space structure to stellar birth separations, we provide a quantitative calibration of how clustered star formation maps onto the evolving phase-space distribution of disc stars. This framework provides a method for co-natal tagging, complementing chemical-abundance and orbital methods in the Milky Way disc. The advent of improved astrometry and radial velocity coverage with *Gaia* DR4 and future spectroscopic surveys will make such comparisons increasingly powerful. Incorporating observational uncertainties into our inference framework, and extending the simulation suite to include additional large-scale perturbations such as the Galactic bar will make this approach directly applicable to real data.

ACKNOWLEDGEMENTS

This research was undertaken with the assistance of resources from the National Computational Infrastructure (NCI Australia) and the Pawsey Supercomputing Centre, NCRIS-enabled capabilities supported by the Australian Government, through award jh2. AA and MRK acknowledge support from the Australian Research Council through Laureate Fellowship FL220100020.

DATA AVAILABILITY

The codes and some of the data used in this study are available at <https://github.com/aruuniima/stellar-actions-II>, along with the complete version of Table 1. The entire simulation outputs are not included in the public repository due to their size, but will be provided by the authors upon reasonable request.

REFERENCES

Abdurro'uf et al., 2022, *ApJS*, **259**, 35
 Antoja T. et al., 2018, *Nature*, **561**, 360
 Antoja T., Ramos P., García-Conde B., Bernet M., Laporte C. F. P., Katz D., 2023, *A&A*, **673**, A115
 Armillotta L., Krumholz M. R., Di Teodoro E. M., McClure-Griffiths N. M., 2019, *MNRAS*, **490**, 4401
 Arora A., Sanderson R. E., Panithampaisal N., Cunningham E. C., Wetzel A., Garavito-Camargo N., 2022, *ApJ*, **939**, 2
 Arunima A., Krumholz M. R., Ireland M. J., Zhang C., Hu Z., 2025, *MNRAS*,
 Bailer-Jones C. A. L., Rybizki J., Fouesneau M., Demleitner M., Andrae R., 2021, *AJ*, **161**, 147
 Baumgardt H., Kroupa P., 2007, *MNRAS*, **380**, 1589
 Binney J., 2012, *MNRAS*, **426**, 1324
 Binney J., Tremaine S., 2008, *Galactic Dynamics: Second Edition*

Bobylev V. V., Bajkova A. T., 2021, *Astronomy Letters*, **47**, 534

Bovy J., 2015, *ApJS*, **216**, 29

Bressan A., Marigo P., Girardi L., Salasnich B., Dal Cero C., Rubele S., Nanni A., 2012, *MNRAS*, **427**, 127

Buder S., et al., 2025, *Publ. Astron. Soc. Australia*, **42**, e051

Castro-Ginard A., et al., 2021, *A&A*, **652**, A162

Chabrier G., 2005, in Corbelli E., Palla F., Zinnecker H., eds, *Astrophysics and Space Science Library* Vol. 327, *The Initial Mass Function 50 Years Later*. p. 41 ([arXiv:astro-ph/0409465](https://arxiv.org/abs/astro-ph/0409465)), doi:10.1007/978-1-4020-3407-7_5

Coronado J., Rix H.-W., Trick W. H., El-Badry K., Rybizki J., Xiang M., 2020, *MNRAS*, **495**, 4098

De Leo M., Massari D., Bellazzini M., Mucciarelli A., Acosta-Tripailao B., Nipoti C., 2025, *arXiv e-prints*, p. [arXiv:2511.05655](https://arxiv.org/abs/2511.05655)

Doherty C. L., Gil-Pons P., Lau H. H. B., Lattanzio J. C., Siess L., 2014, *MNRAS*, **437**, 195

Fragkoudi F., et al., 2019, *MNRAS*, **488**, 3324

Frankel N., Bovy J., Tremaine S., Hogg D. W., 2023, *MNRAS*, **521**, 5917

Freeman K., Bland-Hawthorn J., 2002, *ARA&A*, **40**, 487

Fürnkranz V., Rix H.-W., Coronado J., Seeburger R., 2024, *ApJ*, **961**, 113

Gaia Collaboration et al., 2023, *A&A*, **674**, A1

Gómez F. A., Helmi A., 2010, *MNRAS*, **401**, 2285

Helmi A., de Zeeuw P. T., 2000, *MNRAS*, **319**, 657

Helmi A., Babusiaux C., Koppelman H. H., Massari D., Veljanoski J., Brown A. G. A., 2018, *Nature*, **563**, 85

Hopkins P. F., 2015, *MNRAS*, **450**, 53

Hopkins P. F., 2016, *MNRAS*, **462**, 576

Hopkins P. F., Raives M. J., 2016, *MNRAS*, **455**, 51

Hopkins P. F., et al., 2018, *MNRAS*, **477**, 1578

Hu Z., Wibking B. D., Krumholz M. R., 2023, *MNRAS*, **521**, 5604

Hunt E. L., Reffert S., 2024a, VizieR Online Data Catalog: Improving the open cluster census. III. (Hunt+, 2024), VizieR On-line Data Catalog: J/A+A/686/A42. Originally published in: 2024A&A...686A..42H

Hunt E. L., Reffert S., 2024b, *A&A*, **686**, A42

Kamdar H., Conroy C., Ting Y.-S., Bonaca A., Johnson B., Cargile P., 2019, *ApJ*, **884**, 173

Kamdar H., Conroy C., Ting Y.-S., 2021, *arXiv e-prints*, p. [arXiv:2106.02050](https://arxiv.org/abs/2106.02050)

Karakas A. I., Lugaro M., 2016, *ApJ*, **825**, 26

Khoperskov S., Gerhard O., Di Matteo P., Haywood M., Katz D., Khrapov S., Khoperskov A., Arnaboldi M., 2020, *A&A*, **634**, L8

Kim J.-h., et al., 2016, *ApJ*, **833**, 202

Krumholz M. R., Fumagalli M., da Silva R. L., Rendahl T., Parra J., 2015, *MNRAS*, **452**, 1447

Krumholz M. R., McKee C. F., Bland-Hawthorn J., 2019, *ARA&A*, **57**, 227

Kuhn M. A., Hillenbrand L. A., Sills A., Feigelson E. D., Getman K. V., 2019, *ApJ*, **870**, 32

Lada C. J., Lada E. A., 2003, *ARA&A*, **41**, 57

Leitherer C., et al., 1999, *ApJS*, **123**, 3

Mackereth J. T., et al., 2019, *MNRAS*, **489**, 176

Mikkola D., McMillan P. J., Hobbs D., 2020, *MNRAS*, **495**, 3295

Myeong G. C., Vasiliev E., Iorio G., Evans N. W., Belokurov V., 2019, *MNRAS*, **488**, 1235

Palicio P. A., Recio-Blanco A., Poggio E., Antoja T., McMillan P. J., Spitoni E., 2023, *A&A*, **670**, L7

Roškar R., Debattista V. P., Quinn T. R., Stinson G. S., Wadsley J., 2008, *ApJ*, **684**, L79

Sellwood J. A., 2010, *MNRAS*, **409**, 145

Sellwood J. A., Binney J. J., 2002, *MNRAS*, **336**, 785

Smith B. D., et al., 2017, *MNRAS*, **466**, 2217

Solway M., Sellwood J. A., Schönrich R., 2012, *MNRAS*, **422**, 1363

Steinmetz M., et al., 2020, *AJ*, **160**, 82

Sukhbold T., Ertl T., Woosley S. E., Brown J. M., Janka H. T., 2016, *ApJ*, **821**, 38

Swiggum C., Alves J., D'Onghia E., 2025, *A&A*, **699**, L5

Tepper-García T., Bland-Hawthorn J., Freeman K., 2022, *MNRAS*, **515**, 5951

Tepper-García T., Bland-Hawthorn J., Bedding T. R., Federrath C., Agertz O., 2025, *MNRAS*, **542**, 1987

Tremaine S., Frankel N., Bovy J., 2023, *MNRAS*, **521**, 114

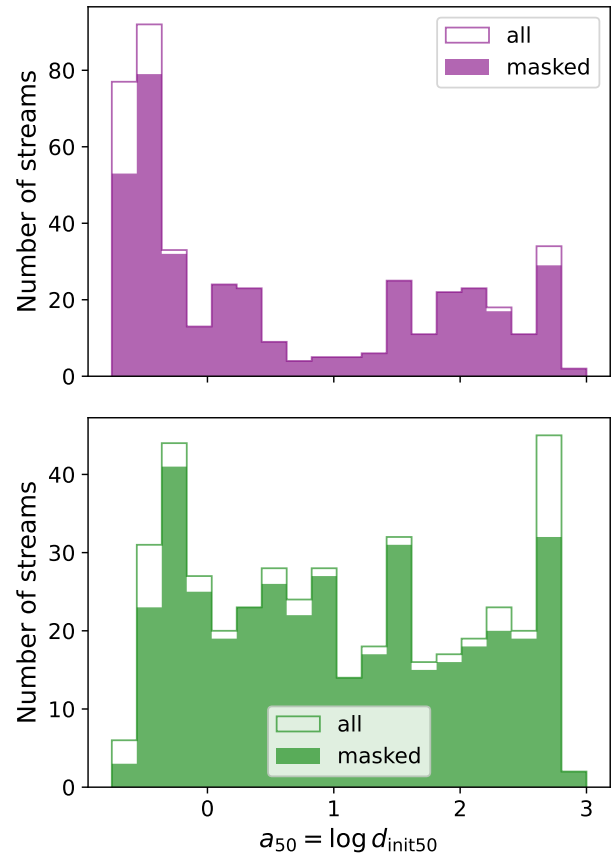


Figure A1. Same as Figure 8 but now showing the 50th percentile of the inferred logarithmic initial sizes (a_{50}) after removing possible outliers from each stream's membership list. Outliers were identified and excluded using a 3σ cut in radial velocity.

Trick W. H., Fragkoudi F., Hunt J. A. S., Mackereth J. T., White S. D. M., 2021, *MNRAS*, **500**, 2645

Vera-Ciro C., D'Onghia E., Navarro J., Abadi M., 2014, *ApJ*, **794**, 173

Vieira K., Korchagin V., Carraro G., Lutsenko A., 2023, *Galaxies*, **11**, 77

Wibking B. D., Krumholz M. R., 2023, *MNRAS*, **521**, 5972

Zhang C., Li Z., Hu Z., Krumholz M. R., 2025, *MNRAS*,

Zucker C., et al., 2022, *Nature*, **601**, 334

da Silva R. L., Fumagalli M., Krumholz M., 2012, *ApJ*, **745**, 145

APPENDIX A: OUTLIERS

This paper has been typeset from a $\text{\TeX}/\text{\LaTeX}$ file prepared by the author.